

# Speedup of high-order unconstrained binary optimization using quantum $\mathbb{Z}_2$ lattice gauge theory

Bi-Ying Wang,<sup>1</sup> Xiaopeng Cui,<sup>1,\*</sup> Qingguo Zeng,<sup>1,2</sup> Yemin Zhan,<sup>1,3</sup> Yu Shi,<sup>4,3,†</sup> and Man-Hong Yung<sup>2,5,6,7,‡</sup>

<sup>1</sup>Quantum Science Center of Guangdong-Hong Kong-Macao Greater Bay Area (Guangdong), Shenzhen, 518129, China

<sup>2</sup>Shenzhen Institute for Quantum Science and Engineering,

Southern University of Science and Technology, Shenzhen, 518055, China

<sup>3</sup>Department of Physics, Fudan University, Shanghai, 200433, China

<sup>4</sup>Shanghai Research Center for Quantum Science and CAS Center for Excellence in Quantum Information and Quantum Physics, University of Science and Technology of China, Shanghai 201315, China

<sup>5</sup>International Quantum Academy, Shenzhen, 518048, China

<sup>6</sup>Guangdong Provincial Key Laboratory of Quantum Science and Engineering,

Southern University of Science and Technology, Shenzhen, 518055, China

<sup>7</sup>Shenzhen Key Laboratory of Quantum Science and Engineering,

Southern University of Science and Technology, Shenzhen, 518055, China

(Dated: June 11, 2024)

How to quickly solve the problem of high-order unconstrained binary optimization (HUBO) has attracted much attention, because of its importance and wide-range applications. Here we implement HUBO using a quantum adiabatic algorithm and achieve algorithmic speedup by introducing gauge symmetry into the algorithm. Gauge symmetry enforces the state to be in the instantaneous ground state, further speeding up the computation. Specifically we map the HUBO problem to quantum  $\mathbb{Z}_2$  lattice gauge theory defined on the dual graph. The gauge operators are found by using the closed-loop-search algorithm, and subsequently the speedup scheme with gauge symmetry for HUBO problem is developed. As an example demonstrated in the classical computers, we present the mathematical formulation of our speedup scheme and propose the so-called gauged local annealing (gLQA), which is the local quantum annealing (LQA) protected by the gauge symmetry. We then use gLQA to calculate the ground state energy of the  $\mathbb{Z}_2$  gauge theory. gLQA reduces the computational time by one order of magnitude from that of LQA.

## I. Introduction

Quadratic unconstrained binary optimization (QUBO) and high-order unconstrained binary optimization (HUBO) are the two high-performance fundamental binary models for the important and wide-range problems of combinatorial optimization. With its simple quadratic-interaction formulation, QUBO has been extensively studied over the past few decades. Numerous classical combinatorial optimization problems, such as Traveling Salesman problem, Boolean Satisfiability problem [1–3], Maximum Likelihood Detection problem in the communication technology [4], error correction based on Low-Density Parity Check, reconfigurable intelligent surfaces beamforming [5], molecular unfolding [6] and protein folding problems [7], as well as the optimal path problem for routes [8], have been successfully converted to QUBO problems.

However, transformation of these problems to QUBO problems necessitates lots of additional variables [9–11] and Rosenberg quadratization penalty terms [12–15], which increase computational costs and make it challenging for the standard optimizations.

In fact, these problems can be naturally expressed in terms of HUBO problems, where the cost functions are polynomials of orders higher than two. Therefore, instead of transforming them to QUBO problems, solving them in HUBO formulation can reduce both the number of binary variables and

the difficulty for model development, thus save computational costs [6, 8, 16–18].

However, still QUBO has attracted more attention than HUBO. The reason is that its quadratic-interaction formulation for binary variables maps to Ising model [19], hence the tremendous amount of knowledge on Ising model has been useful in the design of quantum algorithm and quantum inspired algorithms for QUBO [20–23]. The ground state reached in an adiabatic evolution passing a quantum phase transition corresponds to the optimal solution to the original computational problem.

Therefore, if such quantum approaches are also established for HUBO, it is hopeful to outperform QUBO in this aspect. Here we propose a way to do this, based on the connection with quantum  $\mathbb{Z}_2$  lattice gauge theory (QZ2LGT), which represents another connection between computation and physics. It has been noted that the Hamiltonian of quantum  $\mathbb{Z}_2$  lattice gauge theory (QZ2LGT) [24–27], with high-order interactions, can be studied using the method of quantum simulation [28] and maps to the Hamiltonian Cycle problem [29]. On the other hand, gauge symmetry has already made a significant contribution in quantum error corrections in detecting errors without disrupting the quantum evolution by measuring the conserved quantity with gauge operators [30–32]. We can regard the Hamiltonian of QZ2LGT as a formulation of variable interaction for HUBO, implying the potential of solving HUBO problems by using QZ2LGT.

We can ask the following question. Can we find a method to map HUBO to quantum  $\mathbb{Z}_2$  gauge theory and subsequently leverage the gauge symmetry to improve HUBO solvers?

In the present work, we provide a positive answer to this question. A problem graph of the HUBO is constructed [29],

\* xpclove@126.com

† yu\_shi@ustc.edu.cn

‡ yung@sustech.edu.cn

and the corresponding model of  $\mathbb{Z}_2$  gauge theory is defined on the dual. Afterwards, based on the gauge symmetry, a speedup scheme inspired by quantum Zeno dynamics [33–35] is introduced to improve the quantum adiabatic evolution. The gauge operators commute with the Hamiltonian, hence measurements of the gauge operators cause the state close to be the instantaneous ground state to reduce to the instantaneous ground state with large probabilities. Our algorithm makes use of this to enforce the state to be the instantaneous ground state, hence further speed up the computation.

We apply our method to improve the LQA and propose gLQA. Then, we apply the original LQA and our gLQA to calculate the ground state energy of the quantum  $\mathbb{Z}_2$  gauge theory for 2D lattice and four-regular graph. As a comparison, we also utilize simulated annealing (SA)[36] to calculate the ground state of a 2D lattice, by leveraging the capabilities of the advanced Python package OpenJij[37]. It is shown to be outperformed by LQA and gLQA.

## II. Method

### A. Mapping HUBO to $\mathbb{Z}_2$ gauge theory

In this subsection, we first discuss how to map HUBO to QZ2LGT. Then the method to find out the gauge operators of the corresponding QZ2LGT is presented.

The objective of a HUBO is to minimize

$$H(\mathbf{s}) = \sum_{i_1} J_{i_1} s_{i_1} + \sum_{i_1 < i_2} J_{i_1 i_2} s_{i_1} s_{i_2} + \dots + \sum_{i_1 < i_2 < \dots < i_N} J_{i_1 i_2 \dots i_N} \prod_{j=1}^N s_j, \quad (1)$$

for  $N \geq 3$  with real-number coefficients  $J_s$  and  $\mathbf{s} \in \{-1, 1\}^N$ .

The procedure to map HUBO to QZ2LGT involves three steps. First, we use a graph to describe the HUBO problem, which we refer to as the *HUBO-graph*. In a *HUBO-graph*, one edge denotes one binary spin  $s_i$  of the HUBO, while one vertex represents a term of the HUBO. Second, we map the *HUBO-graph* to its dual, which we refer to as *G-graph*. In this transformation, each vertex in the *HUBO-graph* maps to a plaquette in the *G-graph* and each edge in the *HUBO-graph* is crossed by one link in the *G-graph*, while two adjacent vertices

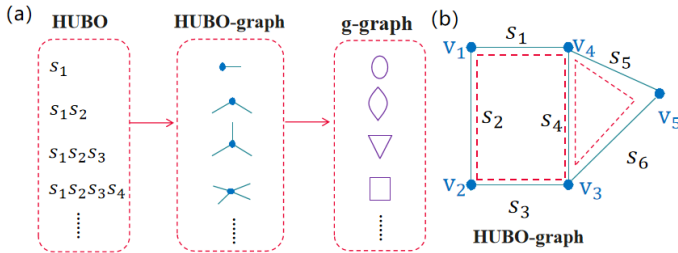


FIG. 1. (a) Four different terms with interaction order varying from 1 to 4 in the objective function of HUBO map to four kinds of vertices in the *HUBO-graph* and four kinds of plaquettes in the *G-graph*. (b) An example of inefficient cycle in the *HUBO-graph*.

in the *HUBO-graph* map to two adjacent plaquettes in the *G-graph*. To illustrate the procedure, we present the mapping from four different terms with interaction order varying from 1 to 4 in the objective function of HUBO to four kinds of vertices of *HUBO-graph* and four kinds of plaquettes of *G-graph* in Fig. 1(a). As seen from the figure, each term in HUBO problem will be mapped to a vertex in the *HUBO-graph* and subsequently to a plaquette in the *G-graph*. Finally, by placing spins at links of this *G-graph*, we build QZ2LGT on the *G-graph* and thus relate the original HUBO with QZ2LGT, with the Hamiltonian

$$\hat{H} = \hat{Z} + g\hat{X}, \quad (2)$$

where  $g$  is the coupling parameter and  $\hat{X} = -\sum_l \hat{\sigma}_x^l$  denotes the  $\hat{\sigma}_x$  operation on all spins.  $\hat{Z} = \sum_p J_p \prod_{l \in p} \hat{\sigma}_z^l$  represents the  $\hat{\sigma}_z$  operating on the spins of all plaquettes. The gauge operator which commutes with Hamiltonian  $\hat{H}$  is defined as the product of  $\hat{\sigma}_x$  on all links of each site  $v$  with

$$\hat{G}_v = \prod_{l \in v} \hat{\sigma}_x^l. \quad (3)$$

The solution to the HUBO problem correspond to the ground state of the Hamiltonian of  $\mathbb{Z}_2$  gauge theory in the  $\hat{\sigma}_z$  basis with  $g = 0$ .

---

#### Algorithm 1 The algorithm to obtain gauge operators

---

**Input:** *HUBO-graph*:  $G_{\text{HUBO}}$ , and the maximum length of cycles  $k_m$   
**Output:** cycle sets  $C = k : C_k$  ( $k = 3, 4, \dots, k_m$ )  
**Function *FindCycleDFS***( $G, k, [v]$ ): return all cycles from vertex  $v$  with length  $k$   
**Function *checkIfSimple***( $P$ ): check if a cycle  $P$  can be divided into smaller cycles  
Initialization:  $k=2$   
1: **while**  $k < k_m$  **do**  
2:    $k \leftarrow k + 1$ ;  
3:   **for**  $v \in G_{\text{HUBO}}$  **do**  
4:      $P_k \leftarrow$ yield from *FindCycleDFS*( $G_{\text{HUBO}}, k, [v]$ );  
5:   **end for**  
6:   **for**  $P \in P_k$  **do**  
7:     **if** *checkIfSimple*( $P$ ) is True **then**  
8:       Add cycle  $P$  to set  $C_k$ ;  
9:     **end if**  
10:   **end for**  
11: **end while**

---

**Algorithm 2** The function *FindCycleDFS*( $G, k, v_p$ )

---

**Input:** Graph  $G$ , cycle length  $k$  and vertices list  $v_p$  in the cycle  
**Output:** cycles with length  $k$  and initial vertex  $v$

```

1: candidate =  $G[v_p[-1]]$ 
2: if length of current vertices in  $v_p$  is equal to  $k$  then
3:   if  $v_p[0]$  in candidate then
4:     cycle  $\leftarrow v_p$ 
5:     yield cycle
6:   end if
7: else if length of current path is smaller than  $k$  then
8:   for  $v \in$  candidate do
9:     if  $v \in v_p$  then
10:      continue
11:    else if then
12:      yield from FindCycleDFS( $G, k, v_p + [v]$ )
13:    end if
14:  end for
15: end if

```

---

**Algorithm 3** The function *checkIfSimple*( $c_t$ )

---

**Input:** Efficient cycle set  $C$  and a cycle  $c_t$  with length  $k_p$   
**Output:** True or False  
**Initialization:**  $k=2$

```

1: while  $k_p - k > 0$  do
2:    $k \leftarrow k + 1$ 
3:   for  $c_i \in C[k]$  do
4:     if  $c_i \subset c_t$  then
5:       return False
6:     end if
7:   end for
8: end while
9: return True

```

---

The  $G$ -graph obtained is complicated, so it is not easy to obtain the gauge operators by directly counting the sites. Since each site on the  $G$ -graph comes from an efficient cycle on the  $HUBO$ -graph, which cannot be separated into two cycles in the dual graph, we search for the efficient cycles in the  $HUBO$ -graph instead. We present our algorithm in Algorithm 1. Conventionally, a graph  $G = \{V, E\}$  is defined with a set of vertices  $V$  and a set of edges  $E$ . In our calculation, the format of the input  $HUBO$ -graph is defined in terms of vertices  $v$  and the adjacent vertices  $v_a$  with  $G_{HUBO} = \{v : \{v_a\}\}$ . For example, if in a graph  $G$  with vertices  $v = \{v_1, v_2, v_3\}$ , the vertex  $v_1$  is connected to vertices  $v_2$  and  $v_3$ , the format of this graph is  $G = \{v_1 : \{v_2, v_3\}, v_2 : \{v_1\}, v_3 : \{v_1\}\}$ . As seen from the algorithm, a function *FindCycleDFS*( $G, k, [v]$ ) is applied to find a cycle set  $p_k$  which contains all cycles from the starting vertex  $v$  with a fixed number of edges  $k$  in the graph  $G$ . This function is based on the depth-first-search algorithm [38], the detail of which is illustrated in Algorithm 2. Not all of these cycles are needed. For example, as seen from the Fig. 1, the blue cycle which contains the vertices  $\{v_1, v_2, v_3, v_4, v_5\}$  can be divided into two small red cycles with vertices  $\{v_3, v_4, v_5\}$  and  $\{v_1, v_2, v_3, v_4\}$ . This cycle does not correspond to a site in the dual graph. To eliminate this kind of cycle, after obtaining a new cycle  $c_t$ , we introduce an additional checking step,

in which we check if there exists a subset  $c_i$  being a cycle. Since we search for the cycles with increasing length  $k$  in the  $HUBO$ -graph and the efficient cycles with shorter length  $k$  have already been collected into the set  $C$ , we check in cycle sets  $C$ , if there exists a cycle that is the subset of the tested cycle  $c_t$ . The detail of the function is illustrated in the Algorithm 3. After obtaining edges  $s$  in the cycle  $c$ , the corresponding gauge operator defined in the  $G$ -graph is known to be

$$\hat{G}_i = \prod_{s \in c} \sigma_x^s \quad (4)$$

**B. Our speedup scheme**

In this subsection, we first introduce our proposed speedup scheme with gauge symmetry. Then, as a specific case calculated on the classical computers, we introduce our gLQA.

Assuming that an operator  $\hat{G}$  and the target Hamiltonian  $\hat{H}$  commute, the ground state of spin configuration  $|\psi_g\rangle = |s_1 \dots s_n\rangle$  of the target Hamiltonian  $\hat{H}$  satisfies

$$\hat{G}|\psi_g\rangle = a|\psi_g\rangle, \quad (5)$$

with constant  $a$ . During the evolution, measurement under the operator  $\hat{G}$  is made on the system, and the correction according to the measurement result  $\langle \psi(t) | \hat{G} | \psi(t) \rangle$  is subsequently made to force the system to its ground state. After this correction process, the system state becomes:

$$|\psi^c(t)\rangle = f(|\psi(t)\rangle, \langle \psi(t) | \hat{G} | \psi(t) \rangle, a), \quad (6)$$

where  $f(|\psi(t)\rangle, \langle \psi(t) | \hat{G} | \psi(t) \rangle, a)$  represents the correction procedure and depends on the correction algorithm. This process is repeated until the state  $|\psi^c(t)\rangle$  becomes the ground state  $|\psi_g\rangle$ . After transforming the problem into the classical binary optimization, the optimization Hamiltonian  $H(\mathbf{s})$  and symmetry operator  $G(\mathbf{s})$  can be described in terms of classical spin configuration  $\mathbf{s}$  which is a vector consisting of  $s_i$ . In our speedup scheme, an symmetry-forced operation based on gradient is made on the spin configuration  $\mathbf{s}$  in every evolution step of quantum algorithm as

$$s_i \leftarrow s_i + B[G(\mathbf{s}) - a] \frac{\partial G(\mathbf{s})}{\partial s_i}, \quad (7)$$

where  $B$  is the evolution parameter to control the symmetry-influenced evolution speed.

*1. Local quantum annealing*

In quantum annealing, one considers a system evolving under the time-dependent Hamiltonian as

$$\hat{H}(t) = t\gamma\hat{H}_t - (1-t)\hat{H}_x, \quad (8)$$

with  $\gamma$  controlling the fraction of the energy of target Hamiltonian  $\hat{H}_t$  in the total Hamiltonian. The system is initially prepared in the state  $|+\rangle^{\otimes n}$ , which is the ground state of the

Hamiltonian  $-\hat{H}_x = -\sum_{i=1}^n \hat{\sigma}_x^i$ , where  $n$  is the number of spins in the system and  $\hat{\sigma}_x^i$  is a Pauli operator on the  $i$ th spin. The Hamiltonian varies from the initial Hamiltonian  $-\hat{H}_x$  at  $t = 0$  to the target Hamiltonian  $\hat{H}_t$  at time  $t = 1$ . If the variation speed of the Hamiltonian is slowly enough to meet the adiabatic condition, the state of the system stays at instantaneous ground state during the evolution, reaching the ground state of the target Hamiltonian finally.

In LQA, which is inspired from quantum annealing, only considers the states of the local form [39]

$$|\theta\rangle = |\theta_1\rangle \otimes |\theta_2\rangle \otimes \dots \otimes |\theta_n\rangle. \quad (9)$$

where  $\theta_i$  denotes the angle between the state of the  $i$ th-spin with the x-axis, and is written in the form

$$|\theta_i\rangle = \cos \frac{\theta}{2} |+\rangle + \sin \frac{\theta}{2} |-\rangle. \quad (10)$$

Thus, we have

$$\begin{aligned} x_i &= \langle \theta_i | \hat{\sigma}_x^i | \theta_i \rangle = \cos \theta_i \\ z_i &= \langle \theta_i | \hat{\sigma}_z^i | \theta_i \rangle = \sin \theta_i. \end{aligned} \quad (11)$$

The cost function of the LQA is defined as:

$$C(t, \theta) = \langle \theta | \hat{H}(t) | \theta \rangle. \quad (12)$$

After substituting Eq. (11) to Eq. (12), the cost function can be written as a function of variable  $\theta$ . Then, a variable  $w_i \in \mathbb{R}$  is applied to parameterise the variable  $\theta_i$  through  $\theta_i = \frac{\pi}{2} \tanh w_i$  in order to limit the variable  $\theta_i \in [-\frac{\pi}{2}, \frac{\pi}{2}]$ . As a result, the cost function  $C(t, \mathbf{w})$  is expressed as a function of variable  $w_i (i = 1, \dots, n)$  and time  $t$ . After discretizing the time to  $t_j = j/N_{\text{iter}} (j = 1, \dots, N_{\text{iter}})$ , an iteration relying on the gradient of cost function is performed to calculate the final spin configuration. After updating the time, the iteration of variables  $w_i$  for all spins is [39]

$$\begin{aligned} \mathbf{v} &\leftarrow \mu \mathbf{v} - \eta \nabla_{\mathbf{w}} C(\mathbf{w}, t) \\ \mathbf{w} &\leftarrow \mathbf{w} + \mathbf{v}, \end{aligned} \quad (13)$$

where  $\mu \in [0, 1]$  is a momentum parameter applied on the momentum variable  $\mathbf{v}$  and  $\eta$  is the step-size of the gradient descent. After the iteration, the final spin configuration can be obtained by using  $s_i = \text{sign}(w_i)$ .  $s_i = \pm 1$  corresponds to the state  $|0\rangle$  or  $|1\rangle$ .

## 2. Local quantum annealing protected by the gauge symmetry

In this subsection, we present the formulation of gLQA by introducing gauge symmetry. During the quantum annealing process, the state is always the instantaneous ground state. Since every gauge operator commutes with the system Hamiltonian, the system state in the adiabatic evolution is also the ground state of the gauge operators. Thus, in the local quantum annealing, we have

$$\hat{G}_i |\theta\rangle = |\theta\rangle. \quad (14)$$

After obtaining the localized classical formula of gauge operator  $G_i = \langle \theta | \hat{G}_i | \theta \rangle$ , an additional gradient-based iteration generated from the gauge operator is applied to force the state to satisfy the gauge symmetry under

$$w_i \leftarrow w_i + B \sum_{v_i} (G_{v_i} - 1) \frac{\partial G_{v_i}}{\partial w_i}, \quad (15)$$

where  $v_i$  represents the sites on link  $i$ , and  $B$  is a constant. By replacing  $G_{v_i}$  with  $\prod_{l \in v_i} x_l$ , the iteration for the gLQA becomes

$$\begin{aligned} v_i &\leftarrow \mu v_i - \eta \nabla_{w_i} C(\mathbf{w}, t) \\ w_i &\leftarrow w_i + v_i \\ w_i &\leftarrow w_i + B \sum_{v_i} \left( \prod_{l \in v_i} x_l - 1 \right) \frac{\partial \prod_{l \in v_i} x_l}{\partial w_i}. \end{aligned} \quad (16)$$

## III. Results

As introduced in Sec. II A, a HUBO task can be mapped to the calculation of the ground state and its energy of the quantum  $\mathbb{Z}_2$  gauge theory on a  $G$ -graph. In order to benchmark our algorithm, we apply LQA and gLQA to calculate the ground energies of two kinds of  $G$ -graph, namely, 2D square lattice and the dual graph of a random four-regular graph. In this subsection, the structures of the two graphs are introduced. Then the calculation results of each graph are presented, which are performed on an Intel® CPU i7-8700 operating at a frequency of 3.2GHz. To benchmark the speed of algorithms, we introduce a standard merit – time to solution (TTS), which is defined as the computation time for finding an optimal value/solution with 99% probability [40, 41]. TTS can be calculated through the real computation time  $t_p$  as

$$\text{TTS} = t_p \frac{\log(1 - 0.99)}{\log(1 - p)}, \quad (17)$$

where probability  $p \equiv \frac{n_{\text{sol}}}{n_{\text{sam}}}$  denotes the ratio between number of times  $n_{\text{sol}}$  achieving the ground energy to the total number of sampling times  $n_{\text{sam}}$  in corresponding computation time  $t_p$ .

### A. 2D lattice and four-regular graph

On a square lattice of size  $L \times L$ , there are  $2L^2$  links and  $L^2$  plaquettes. In the lattice, one spin locates at each link, so altogether there are  $N = 2L^2$  spins,  $N_p = L^2$  plaquettes and  $N_v = L^2$  vertices. The Hamiltonian of  $\mathbb{Z}_2$  lattice gauge theory is as in Eq. (2). The lattice is depicted in Fig. 2(a). As seen from the figure, each magnetic term contains  $\hat{\sigma}_z$  operating on the four spins ( $p1, p2, p3, p4$ ) of one plaquette with  $\hat{Z} = -\sum_p \hat{\sigma}_x^{p1} \hat{\sigma}_x^{p2} \hat{\sigma}_x^{p3} \hat{\sigma}_x^{p4}$ , while the gauge operator  $\hat{G}_v$  contains four links of site  $v$  and can be written as  $\hat{G}_v = \hat{\sigma}_x^{v1} \hat{\sigma}_x^{v2} \hat{\sigma}_x^{v3} \hat{\sigma}_x^{v4}$ .

We generate a random  $G$ -graph by finding the dual lattice of a random four-regular graph as presented in Fig. 2(b). As seen from the figure, every edge in the four-regular graph maps



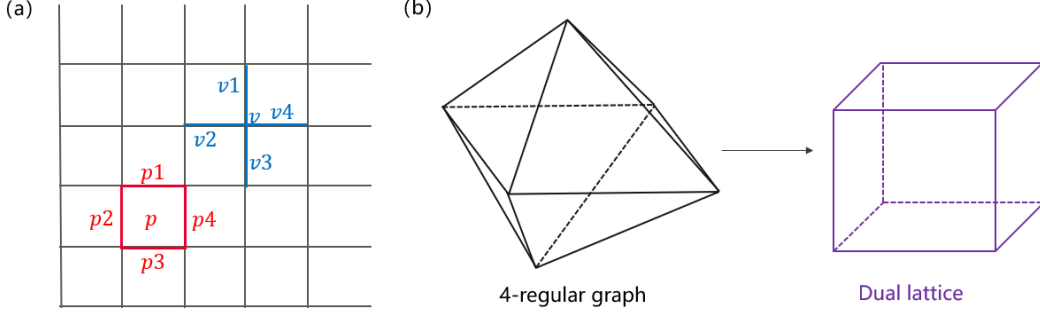


FIG. 2. (a) The structure of a square lattice. (b) The  $G$ -graph obtained as the dual lattice of a four-regular graph.

to one link in the  $G$ -graph which crosses the edge, and every vertex or site in the four-regular graph maps to a plaquette in the  $G$ -graph, an efficient cycle in the four-regular graph maps to a site in the  $G$ -graph. As explained in Sec. II A, by counting all the vertices, the operator  $\hat{Z}$  (gauge operator  $G_v$ ) of the  $G$ -graph can be obtained. In the four-regular graph, each vertex has four connected edges, which consequently lead to four links  $\{p1, p2, p3, p4\}$  in every plaquette  $p$  of the obtained  $G$ -graph. Thus, the  $\hat{Z}$  operator can be written as  $\hat{Z} = -\sum_p \hat{\sigma}_x^{p1} \hat{\sigma}_x^{p2} \hat{\sigma}_x^{p3} \hat{\sigma}_x^{p4}$ . Due to the uncertain length of the cycle in a randomly generated four-regular graph, the number of links in one site  $s$  of  $G$ -graph is uncertain. For convenience, in the following calculation, we only collect the gauge operators for which the number of spins included is smaller than a threshold  $k_m$  for the  $G$ -graphs generated by four-regular graphs.

## B. Numerical results for 2D lattices

In this subsection, we present our results obtained for a square lattice through the optimization process using our gLQA. We initially discuss the results for a lattice size  $L = 10$ , before present the results for a range of lattice sizes from 10 to 40. For comparison, we also include the results of optimization from LQA. In addition, for  $L = 10$ , optimization from SA is also presented.

A lattice contains  $N_p = L^2$  plaquettes, so the ground state energy  $E_s$  is  $E_s = -N_p$ . The minimum energy  $E_{\min}$  and median energy  $E_{\text{med}}$ , which is the median values of the energy over all the samples, as functions of the number of iteration steps  $n_{\text{iter}}$ , for sampling number of times  $n_{\text{sam}} = 200$  and lattice size  $L = 10$ , are depicted in Fig. 3(a) and Fig. 3(b), respectively. As can be seen from Fig. 3(a) and Fig. 3(b), though  $E_{\min}$  and  $E_{\text{med}}$  obtained from SA (green curve in the figures) exhibit rapid decreases and subsequent saturation with the increase of iteration steps  $n_{\text{iter}}$ , the results fail to converge to the ground state within 200 times of sampling. As seen from Fig. 3(a), as  $n_{\text{iter}}$  increases,  $E_{\min}$  obtained from LQA

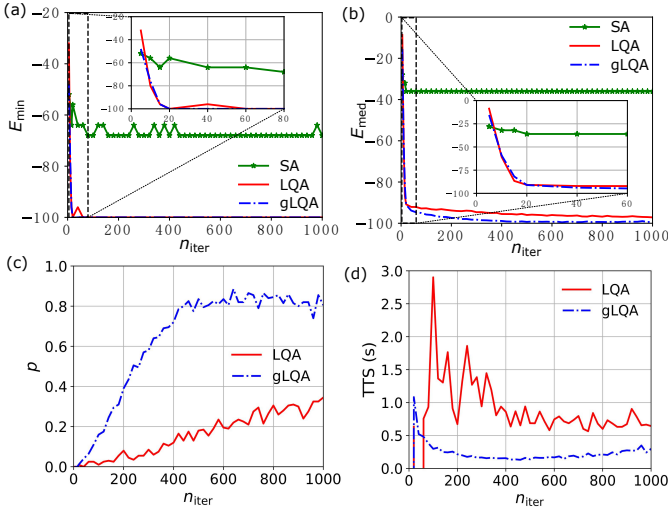


FIG. 3. (a) Minimum energy  $E_{\min}$ , (b) medium energy  $E_{\text{med}}$ , (c) probability  $p$ , (d) TTS, as functions of iteration steps  $n_{\text{iter}}$  for a square lattice with  $L = 10$ . The results obtained from LQA, gLQA and SA are all based on sampling number of times  $n_{\text{sam}} = 200$ .

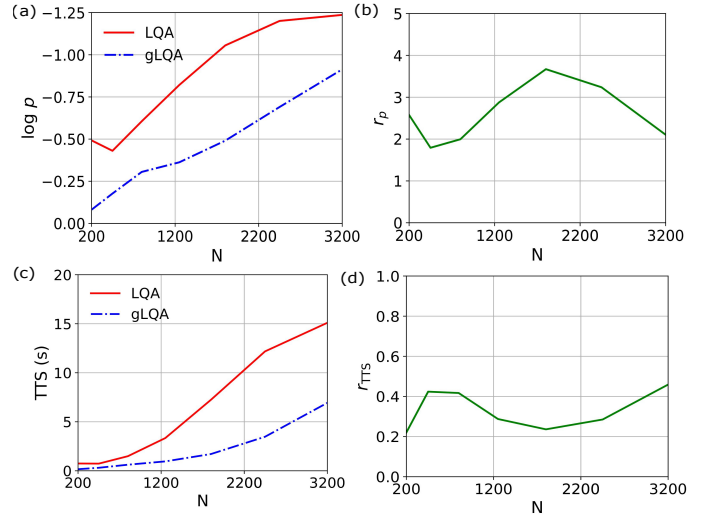


FIG. 4. (a) Success probability  $p$ , (b) ratio  $r_p$ , (c) TTS, (d) ratio  $r_{\text{TTS}}$  as functions of spin number  $N$  for square lattices.

and that from gLQA rapidly decrease and saturate towards the ground state energy  $E_s = -100$  within sixty steps of iteration. Moreover,  $E_{\min}$  obtained from gLQA reaches the ground state energy quicker than LQA. As seen from Fig. 3(b), similar behavior can be observed for  $E_{\text{med}}$  calculated from LQA and that from gLQA, which swiftly decrease before gradually slow down until saturate. Besides,  $E_{\text{med}}$  obtained from gLQA is lower than that from LQA. The probability  $p$  and TTS as functions of iteration step  $n_{\text{iter}}$  are illustrated in the Fig. 3(c) and (d) respectively. As seen from Fig. 3(c), the probability  $p$  calculated from gLQA and that from LQA gradually increase with  $n_{\text{iter}}$ , leading to the decrease of TTS in the Fig. 3(d). For  $n_{\text{iter}} \geq 500$ , the probability  $p$  calculated in gLQA saturates to a high value  $\sim 0.81$ , inducing a slow increase of TTS with  $n_{\text{iter}}$ . The probability  $p$  calculated in LQA saturates to  $p \sim 0.35$  for  $n_{\text{iter}} \geq 1000$ . It is clearly seen in Fig. 3(d) that our gLQA achieves shorter TTS than LQA. Notably, the shortest TTS of approximately 0.15 s for our gLQA for this lattice occurs at  $n_{\text{iter}} = 500$ , which is less than a quarter of the shortest TTS of approximately 0.60 s for LQA, demonstrating a fourfold increase of the speed by using our gLQA.

The results with  $n_{\text{sam}} = 1000$  for lattices with various values of spin number  $N$  (size  $L$  ranging from 10 to 40) are illustrated in Fig. 4. Since the results obtained from SA cannot reach the ground state for a small lattice with  $L = 10$ , we only focus on the comparison between LQA and gLQA in the following part. With the increase of spin number  $N$ , for the iteration step fixed at 1000, the probability  $p$  in Fig. 4(a) decreases, which consequently leads to the increased TTS in the Fig. 4(c). To make a clear comparison, the  $N$  dependence of ratio  $r_p$  ( $r_{\text{TTS}}$ ) between the success probability (TTS) calculated in our gLQA and that in LQA is presented in the Fig. 4(b) (Fig. 4(d)). The figures clearly indicate that our gLQA method achieves at least a twofold increase in probability  $p$  and a reduction of TTS by 60%.

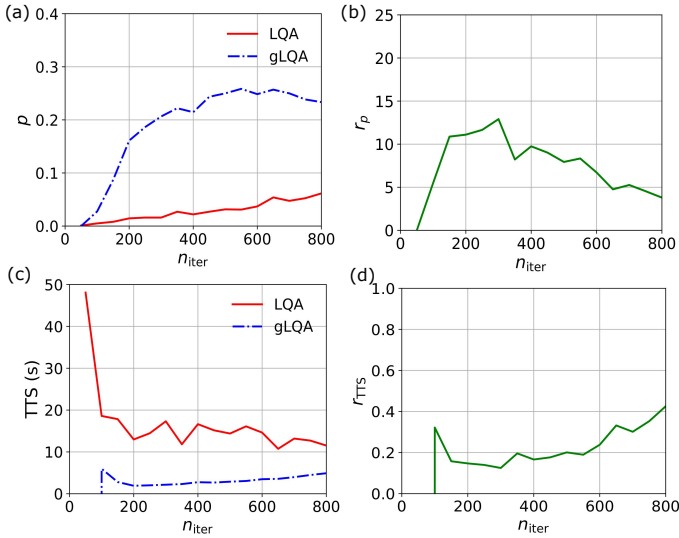


FIG. 5. (a) Success probability  $p$ , (b) ratio  $r_p$ , (c) TTS, (d) ratio  $r_{\text{TTS}}$ , as functions of iteration steps  $n_{\text{iter}}$  for a  $G$ -graphs transformed from a random four-regular graph with spin number  $N = 200$ .

### C. Results for $G$ -graphs generated from four-regular graphs

In this subsection, we present our results for  $G$ -graphs generated from four-regular graphs. We initially discuss the results for a  $G$ -graph with  $N = 200$ . Then, the outcomes for  $N$  ranging from 200 to 800 are presented.

The calculated success probability and TTS as functions of the number of iteration steps  $n_{\text{iter}}$ , for sampling number of times  $n_{\text{sam}} = 2000$  for a random  $G$ -graph with 200 links, are shown in the Fig. 5(a) and Fig. 5(c). As seen from the Fig. 5(a), with the increase of  $n_{\text{iter}}$ , the success probability  $p$  in LQA and that in gLQA both start to gradually increase from 0 for iteration steps larger than 100. Then the success probability  $p$  in gLQA saturates around 0.25 for  $n_{\text{iter}} \geq 500$ , while success probability  $p$  in LQA has just saturated and only reaches  $\sim 0.05$  for  $n_{\text{iter}} = 800$ . Due to the zero probability  $p = 0$  for  $n_{\text{iter}} < 100$ , TTS in this regime is meaningless in Fig. 5(c). As seen from Fig. 5(c), with the increase of  $n_{\text{iter}}$ , TTS' in both LQA and gLQA first decrease, thanks to the increase of probability  $p$ , then start to gradually increase due to the increasing computation time  $t_p$ . It is notable that the shortest TTS in LQA is around 11s, which is more than fivefold of the one in our gLQA, which is  $\sim 2$  s. The ratios  $r_p$  and  $r_{\text{TTS}}$  as functions of  $n_{\text{iter}}$  are shown respectively in the Fig. 5(b) and Fig. 5(d). Fig. 5(b) displays at least a fourfold increase of the success probability by our gLQA, which reaches thirteenfold at  $n_{\text{iter}} = 300$ . As shown in Fig. 5(d), TTS in our gLQA has a  $\sim 60\%$  reduction compared with the one from LQA, which reaches  $\sim 85\%$  at  $n_{\text{iter}} = 300$ . The results with  $n_{\text{sam}} = 100000$  for  $G$ -graph generated from four-regular graphs with spin number  $N$  ranging from 200 to 800 are presented in Fig. 6. With the increase of spin number  $N$ , for the iteration step kept constant at 500, the success probability  $p$  decreases, as shown in Fig. 6(a), and consequently leads to the increase of TTS, as shown in the Fig. 6(c). Besides, a sudden increase

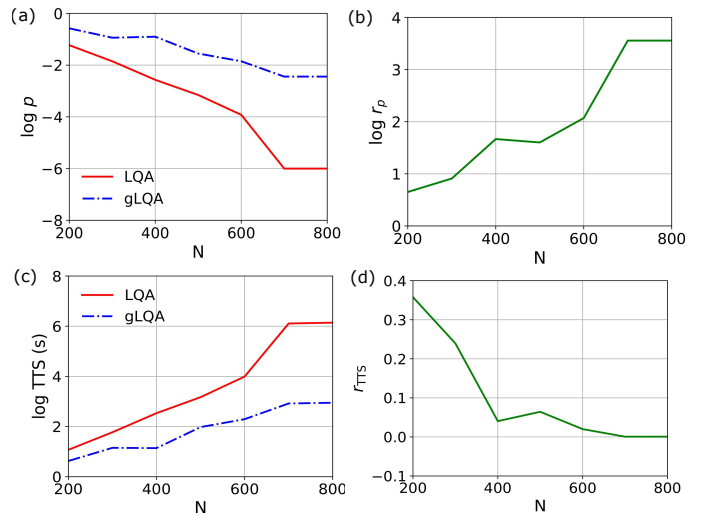


FIG. 6. (a) Success probability  $p$ , (b) ratio  $r_p$ , (c) TTS, (d) ratio  $r_{\text{TTS}}$ , as functions of spin number  $N$  for the  $G$ -graphs transformed from random four-regular graphs.

of TTS in LQA appears due to the near-zero probability  $p$  for  $N > 600$ . To make a clear comparison,  $N$  dependences of ratio  $r_p$  and  $r_{\text{TTS}}$  are presented in Fig. 6(b) and Fig. 6(d). The figures clearly indicate that our gLQA method achieves an obvious increase in probability  $p$ , while displays a reduction of TTS larger than 75%. For large  $G$ -graph with  $N > 600$ , the increase of success probability for our gLQA can be larger than 3000 and the reduction of TTS can reach three orders of magnitude.

#### IV. Conclusion and discussion

In this paper, we have established a quantum approach to HUBO by mapping it to a graph problem, which is subsequently transformed to QZ2LGT defined on the dual graph, referred to as the  $G$ -graph. This graph transformation allows us to link the HUBO with the  $\mathbb{Z}_2$  gauge theory and introduces a method of identifying the corresponding gauge operators. The process of solving HUBO is thus transformed into finding the ground state and its energy in the  $\mathbb{Z}_2$  gauge theory. The gauge operators commute with the Hamiltonian, hence enforce the state to be in ground state during its evolution, leading to the speedup of the adiabatic algorithm. Based on this, we have proposed a speedup scheme for quantum-inspired algorithms, facilitated by the gauge symmetry, and introduced a gauge-

forced iteration step to further speed up the computation.

We have demonstrated the advantage of our method by its application to enhance the LQA and introducing the gLQA. We have conducted benchmarking for LQA and gLQA on two types of  $G$ -graphs with spin numbers ranging from 200 to 3200. For comparison, we have also applied SA to solve these problems. Since the key to find the optimal solution of a HUBO problem is to find the ground state, SA fails even for a small 2D lattice with size  $L = 10$ . Our benchmarking of TTS based on LQA and gLQA demonstrated that gLQA significantly outperforms LQA.

There are several potential avenues for future developments. It would be beneficial to test our speedup scheme on a wider range of instances and develop an automated technique for tuning the parameters in our scheme, such as constant  $B$  and the time step. Currently, these parameters are determined through preliminary search in our work, which is not feasible for real-world applications. In this study, we have successfully identified  $\mathbb{Z}_2$  gauge theory as suitable for HUBO and leveraged gauge symmetry to expedite the solution process. This is the first and proof-of-principle in the field. However, here we have only utilized the gauge symmetry to speed up the solution. Other physical features of the  $\mathbb{Z}_2$  theory could also be applied to enhance HUBO solutions, as new directions in this field.

**Acknowledgements** This work was supported by National Natural Science Foundation of China (Grant No. 12075059).

- 
- [1] A. Lucas, Ising formulations of many np problems, *Front. Phys.* **2**, 4 (2014).
  - [2] K. P. Kalinin and N. G. Berloff, Computational complexity continuum within Ising formulation of NP problems, *Commun Phys* **5**, 20 (2022).
  - [3] N. Mohseni, P. L. McMahon, and T. Byrnes, Ising machines as hardware solvers of combinatorial optimization problems, *Nat Rev Phys* **4**, 363 (2022).
  - [4] M. Kim, D. Venturelli, and K. Jamieson, Leveraging quantum annealing for large mimo processing in centralized radio access networks, in *Proceedings of the ACM special interest group on data communication* (2019) pp. 241–255.
  - [5] C. Ross, G. Gradoni, Q. J. Lim, and Z. Peng, Engineering reflective metasurfaces with ising hamiltonian and quantum annealing, *IEEE Trans. Antennas Propagat.* **70**, 2841 (2022).
  - [6] K. Mato, R. Mengoni, D. Ottaviani, and G. Palermo, Quantum molecular unfolding, *Quantum Sci. Technol.* **7**, 035020 (2022).
  - [7] A. Robert, P. K. Barkoutsos, S. Woerner, and I. Tavernelli, Resource-efficient quantum algorithm for protein folding, *npj Quantum Inf* **7**, 38 (2021).
  - [8] A. Glos, A. Krawiec, and Z. Zimborás, Space-efficient binary optimization for variational quantum computing, *npj Quantum Inf* **8**, 39 (2022).
  - [9] R. Xia, T. Bian, and S. Kais, Electronic structure calculations and the ising hamiltonian, *The Journal of Physical Chemistry B* **122**, 3384 (2017).
  - [10] Y. Boykov and V. Kolmogorov, An experimental comparison of min-cut/max-flow algorithms for energy minimization in vision, *IEEE transactions on pattern analysis and machine intelligence* **26**, 1124 (2004).
  - [11] J. Fujisaki, H. Oshima, S. Sato, and K. Fujii, Practical and scalable decoder for topological quantum error correction with an ising machine, *Physical Review Research* **4**, 043086 (2022).
  - [12] I. G. Rosenberg, Reduction of bivalent maximization to the quadratic case, (1975).
  - [13] M. Ayodele, Penalty weights in QUBO formulations: Permutation problems (Springer International Publishing) pp. 159–174.
  - [14] M. D. García, M. Ayodele, and A. Moraglio, Exact and sequential penalty weights in quadratic unconstrained binary optimisation with a digital annealer (Association for Computing Machinery, New York, NY, USA, 2022) p. 184–187.
  - [15] A. Verma and M. Lewis, Penalty and partitioning techniques to improve performance of qubo solvers, *Discrete Optimization* **44**, 100594 (2022).
  - [16] N. Ide, T. Asayama, H. Ueno, and M. Ohzeki, Maximum likelihood channel decoding with quantum annealing machine, in *2020 International Symposium on Information Theory and Its Applications (ISITA)* (IEEE, 2020) pp. 91–95.
  - [17] M. Norimoto, R. Mori, and N. Ishikawa, Quantum algorithm for higher-order unconstrained binary optimization and mimo maximum likelihood detection, *IEEE Transactions on Communications* **71**, 1926 (2023).
  - [18] M. Blondel, A. Fujino, N. Ueda, and M. Ishihata, Higher-order factorization machines (Curran Associates Inc., Red Hook, NY, USA, 2016) p. 3359–3367.
  - [19] F. Barahona, On the computational complexity of ising spin glass models, *Journal of Physics A: Mathematical and General* **15**, 3241 (1982).
  - [20] H. Goto, K. Tatsumura, and A. R. Dixon, Combinatorial optimization by simulating adiabatic bifurcations in nonlinear hamiltonian systems, *Sci. Adv.* **5**, eaav2372 (2019).
  - [21] S. Reifenstein, S. Kako, F. Khoiratee, T. Leleu, and Y. Ya-

- mamoto, Coherent ising machines with optical error correction circuits, *Advanced Quantum Technologies* **4**, 2100077 (2021).
- [22] T. Leleu, F. Khoystatee, T. Levi, R. Hamerly, T. Kohno, and K. Aihara, Scaling advantage of chaotic amplitude control for high-performance combinatorial optimization, *Commun Phys* **4**, 266 (2021).
- [23] F. P. McGeoch, C., *The D-wave advantage system: an overview*, Tech. Rep. (D-Wave Systems Inc, Burnaby, BC, Canada, 2020).
- [24] S. Sachdev, Topological order, emergent gauge fields, and Fermi surface reconstruction, *Rep. Prog. Phys.* **82**, 014001 (2019).
- [25] X. G. Wen, Mean-field theory of spin-liquid states with finite energy gap and topological orders, *Phys. Rev. B* **44**, 2664 (1991).
- [26] X.-G. Wen, Quantum orders and symmetric spin liquids, *Phys. Rev. B* **65**, 165113 (2002).
- [27] A. Hamma and D. A. Lidar, Adiabatic Preparation of Topological Order, *Phys. Rev. Lett.* **100**, 030502 (2008).
- [28] X. Cui, Y. Shi, and J.-C. Yang, Circuit-based digital adiabatic quantum simulation and pseudoquantum simulation as new approaches to lattice gauge theory, *J. High Energ. Phys.* **2020** (8), 160.
- [29] X. Cui and Y. Shi, Correspondence between Hamiltonian Cycle Problem and the Quantum  $\mathbb{Z}_2$  Lattice Gauge Theory, *EPL* **144**, 48001 (2023).
- [30] A. Kitaev, Fault-tolerant quantum computation by anyons, *Annals of Physics* **303**, 2 (2003).
- [31] H. Zhang, L. Wan, S. Paesani, A. Laing, Y. Shi, H. Cai, X. Luo, G.-Q. Lo, L. C. Kwek, and A. Q. Liu, Encoding Error Correction in an Integrated Photonic Chip, *PRX Quantum* **4**, 030340 (2023).
- [32] V. V. Sivak, A. Eickbusch, B. Royer, S. Singh, I. Tsioutsios, S. Ganjam, A. Miano, B. L. Brock, A. Z. Ding, L. Frunzio, S. M. Girvin, R. J. Schoelkopf, and M. H. Devoret, Real-time quantum error correction beyond break-even, *Nature* **616**, 50 (2023).
- [33] D. Herman, R. Shaydulin, Y. Sun, S. Chakrabarti, S. Hu, P. Minssen, A. Rattew, R. Yalovetzky, and M. Pistoia, Constrained optimization via quantum zeno dynamics, *Commun Phys* **6**, 219 (2023).
- [34] F. Schäfer, I. Herrera, S. Cherukattil, C. Lovecchio, F. Cataliotti, F. Caruso, and A. Smerzi, Experimental realization of quantum zeno dynamics, *Nat Commun* **5**, 3194 (2014).
- [35] P. Facchi, G. Marmo, and S. Pascazio, Quantum zeno dynamics and quantum zeno subspaces, *J. Phys.: Conf. Ser.* **196**, 012017 (2009).
- [36] S. K. et al, Optimization by simulated annealing, *Science* **220**, 671 (1983).
- [37] The Comapny Jij, *OpenJij*, Software (2024), version0.9.2.
- [38] R. L. R. T. H. Cormen, C. E. Leiserson and C. Stein, *Introduction to Algorithms*, 3rd ed. (The MIT Press, 2009).
- [39] J. Bowles, A. Dauphin, P. Huembeli, J. Martinez, and A. Acín, Quadratic unconstrained binary optimization via quantum-inspired annealing, *Phys. Rev. A* **18**, 034016 (2022).
- [40] R. Hamerly, T. Inagaki, P. L. McMahon, D. Venturelli, A. Marandi, T. Onodera, E. Ng, C. Langrock, K. Inaba, T. Honjo, K. Enbutsu, T. Umeki, R. Kasahara, S. Utsunomiya, S. Kako, K. ichi Kawarabayashi, R. L. Byer, M. M. Fejer, H. Mabuchi, D. Englund, E. Rieffel, H. Takesue, and Y. Yamamoto, Experimental investigation of performance differences between coherent ising machines and a quantum annealer, *Science Advances* **5**, eaau0823 (2019).
- [41] M. Aramon, G. Rosenberg, E. Valiante, T. Miyazawa, H. Tamura, and H. G. Katzgraber, Physics-inspired optimization for quadratic unconstrained problems using a digital annealer, *Frontiers in Physics* **7**, 48 (2019).